Article

Developmental Cell

Cortical Tension Allocates the First Inner Cells of the Mammalian Embryo

Graphical Abstract

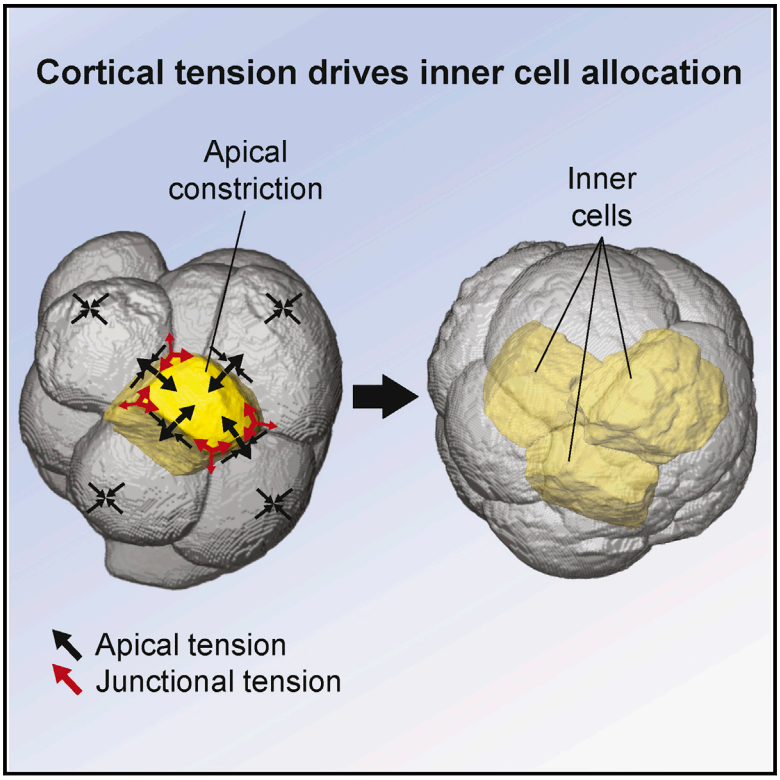

Highlights

- Apical constriction allocates the first inner cells of the mouse embryo
- Myosin II accumulates around constricting cells and is needed for their allocation
- Subcellular heterogeneities in tensile forces determine inner cell allocation
- Neighboring cells dissipate tensile forces required by constricting cells

Authors

Chaminda R. Samarage, Melanie D. White, Yanina D. Álvarez, ..., Stephanie Bissiere, Andreas Fouras, Nicolas Plachta

Correspondence

andreas.fouras@monash.edu (A.F.), plachtan@imcb.a-star.edu.sg (N.P.)

In Brief

Samarage et al. show how mechanical forces form the early mouse embryo. They show that anisotropies in cortical tension—a force generated by contractility of the actomyosin cell cortex—drive the first spatial segregation of cells into the inner regions of the embryo during mammalian development.

Samarage et al., 2015, Developmental Cell *34*, 1–13
August 24, 2015
http://dx.doi.org/10.1016/j.devcel.2015.07.004

CellPress

Please cite this article in press as: Samarage et al., Cortical Tension Allocates the First Inner Cells of the Mammalian Embryo, Developmental Cell (2015), http://dx.doi.org/10.1016/j.devcel.2015.07.004

Developmental Cell
Article

Cortical Tension Allocates the First Inner Cells of the Mammalian Embryo

Chaminda R. Samarage,[1,5] Melanie D. White,[2,5] Yanina D. Álvarez,[2,5] Juan Carlos Fierro-González,[2] Yann Henon,[1] Edwin C. Jesudason,[3] Stephanie Bissiere,[2,4] Andreas Fouras,[1,*] and Nicolas Plachta[2,4,*]
[1]Laboratory for Dynamic Imaging, Faculty of Engineering, Monash University, Clayton Campus, Melbourne, VIC 3800, Australia
[2]EMBL Australia, ARMI, Monash University, Clayton Campus, Melbourne, VIC 3800, Australia
[3]National Health Service, Edinburgh, Scotland EH1 3EG, UK
[4]Institute of Molecular and Cell Biology, A*STAR, 61 Biopolis Drive, Singapore 138673, Singapore
[5]Co-first author
*Correspondence: andreas.fouras@monash.edu (A.F.), plachtan@imcb.a-star.edu.sg (N.P.)
http://dx.doi.org/10.1016/j.devcel.2015.07.004

SUMMARY

Every cell in our body originates from the pluripotent inner mass of the embryo, yet it is unknown how biomechanical forces allocate inner cells in vivo. Here we discover subcellular heterogeneities in tensile forces, generated by actomyosin cortical networks, which drive apical constriction to position the first inner cells of living mouse embryos. Myosin II accumulates specifically around constricting cells, and its disruption dysregulates constriction and cell fate. Laser ablations of actomyosin networks reveal that constricting cells have higher cortical tension, generate tension anisotropies and morphological changes in adjacent regions of neighboring cells, and require their neighbors to coordinate their own changes in shape. Thus, tensile forces determine the first spatial segregation of cells during mammalian development. We propose that, unlike more cohesive tissues, the early embryo dissipates tensile forces required by constricting cells via their neighbors, thereby allowing confined cell repositioning without jeopardizing global architecture.

INTRODUCTION

Although humans and mice originate from pluripotent cells in the inner mass of the embryo, the physical processes initiating the formation of this structure are unknown. It has been theorized that biomechanical forces might play a role in controlling cell allocation during early mammalian development. However, the early embryo is composed of few cells without extracellular matrix contact, and it has remained challenging to probe mechanical forces acting during these early developmental stages. Initially, differences in cell adhesion, typically mediated by E-cadherin, were proposed to explain how the early mouse embryo forms (Kimber et al., 1982). This would be in line with other cell sorting processes based on differential adhesion mechanisms (Fagotto, 2014; Heisenberg and Bellaïche, 2013; Lecuit and Lenne, 2007). Yet thus far it remains unclear whether inner cells differentially regulate E-cadherin levels or dynamics. Others hypothesized that cortical tension, mediated by contractility of actomyosin networks, might also play a role (Anani et al., 2014; Yamanaka et al., 2010). However, these suggestions were mostly based on differences in cell curvature or phosphorylated-myosin II in disaggregated blastomeres (Anani et al., 2014), which cannot recapitulate the spatiotemporal distribution of forces acting within a living embryo.

Furthermore, even the nature of the morphogenetic event(s) giving rise to the first inner cells of the embryo remains unclear. Traditional views still assume that ''asymmetric'' cell divisions allocate inner cells by cleaving the parental cells perpendicular to the embryo surface and positioning one daughter inside, as a direct result of the scission (Johnson and Ziomek, 1981; Wennekamp et al., 2013; Yamanaka et al., 2006; Zernicka-Goetz et al., 2009) (Figure 1A). Yet division-independent routes of inner cell allocation, qualitatively described as cell internalization (Anani et al., 2014), engulfment (Plusa et al., 2005; Yamanaka et al., 2010), jostling (Watanabe et al., 2014), or falling inward (McDole et al., 2011), were suggested to also contribute varying numbers of inner cells.

Understanding the origin of inner cells and the contribution of cell adhesion and cortical tension during early development would require the non-invasive study and quantification of (1) the precise changes in cell shape and position, (2) the distribution of molecules mediating these biomechanical forces, and (3) the magnitude and directionality of the forces acting within the living embryo. Here, we develop high-resolution membrane segmentation to show that inner cells originate primarily by cell internalization events, which we identify as apical constriction. We then combine live imaging, computational analysis, and molecular manipulations to demonstrate that myosin II, but not E-cadherin, selectively accumulates around constricting cells to drive them inside the embryo. Finally, we apply femtosecond laser ablations of actomyosin networks to demonstrate how heterogeneities in the subcellular distribution of tensile forces control inner cell allocation.

RESULTS

Apical Constriction Is the Prime Process Allocating the First Inner Cells of the Embryo

Resolving the origin of inner cells requires quantitative analysis of cell morphology and division in 4D using computational

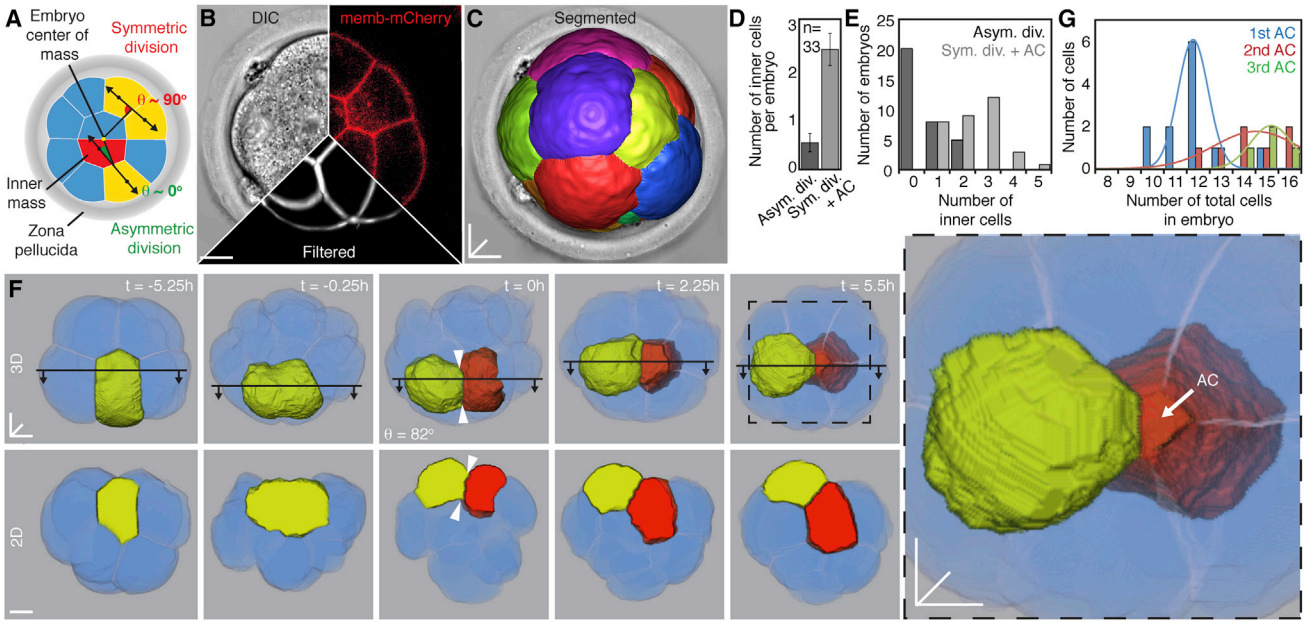

Figure 1. Apical Constriction Allocates the First Inner Cells of the Embryo

(A) Schematic of cell divisions in the early embryo.

(B) Computational membrane segmentation in living mouse embryos expressing memb-mCherry imaged with 4D two-photon microscopy. Membranes are computationally filtered to segment each cell.

(C) Fully segmented living embryo.

(D) Quantification of inner cells generated by asymmetric cell division (Asym. div.) or symmetric division followed by apical constriction (Sym. Div. + AC) ($p < 0.0001$) during the 8- to 16-cell stage.

(E) Distribution of embryos allocating different numbers of inner cells by asymmetric division (dark bars) or apical constriction (AC, light bars). Twenty embryos had no inner cells arising from asymmetric division (dark gray bar = 20), and zero embryos had no inner cells resulting from AC (light gray bar = 0), n = 33 embryos.

(F) Time frames of segmented living embryo show parental cell (yellow) dividing symmetrically and one daughter cell (red) subsequently undergoing apical constriction. The dashed box highlights AC.

(G) Histogram of the number of cells undergoing first, second, and third apical constriction process at different developmental stages, represented by the number of total cells in the embryo.

Data are represented as mean ± SEM. θ represents the division angle; n represents number of embryos. Scale bars represent 10 μm. See also Figures S1 and S2.

membrane segmentation. This approach has proven useful to investigate morphogenetic processes in *Drosophila* (Gelbart et al., 2012) and plant (Yoshida et al., 2014) embryos. However, in mouse embryos, it has only been applied to low-resolution microscopy datasets. Furthermore, there has been no direct demonstration of how a computationally segmented cell undergoes internalization (Watanabe et al., 2014). Therefore, we designed a membrane segmentation method to track all cells in living mouse embryos in 4D at high resolution (Figures 1B and 1C; Movie S1).

We microinjected RNA for membrane-targeted mCherry (memb-mCherry) and imaged embryos with 4D two-photon microscopy. Asymmetric divisions are defined according to convention, as cleavages with angles of <30° (see Experimental Procedures and Figure S1) (Dard et al., 2009). In line with some previous reports (McDole et al., 2011; Yamanaka et al., 2010), we find that most inner cells (81.4%) originate from symmetric divisions (Figure 1D). Moreover, 60.6% of 8- to 16-cell stage embryos (n = 33 embryos) produce inner cells without featuring any asymmetric divisions (Figure 1E, dark colored bars). In the remaining 39.4% of embryos where asymmetric divisions do occur, they typically contribute only one internalized cell (61.5% of those cases). Therefore, asymmetric division is uncommon and unnecessary for positioning the first inner cells of the embryo. Our results agree with a model where the angles of division are randomly defined in 3D. In this 3D model, the probability of a division angle is proportional to the spherical zone, or stripe, at that angle (Dard et al., 2009). Random divisions in 2D result in a 33.33% chance for an asymmetric division, whereas in 3D, an asymmetric division has only a 13.4% chance of occurring (Figure S1).

Tracking our computationally segmented cells reveals that the primary morphogenetic mechanism generating inner cells is apical constriction (Martin and Goldstein, 2014). This process requires 5 ± 2 hr and is characterized by a decrease in apical surface area, an increase in basolateral area, and gradual cell repositioning closer to the embryo center (Figures 1F and 2; Movie S2). In 56% of cases, cells positioning inside the embryo start to constrict 0.50 ± 0.25 hr after their own division (n = 14 embryos, Figures 2C and 2G). In these cases, the cell that constricts is positioned closer to the embryo's center following division (Figures 2E and 2F). In the remaining 44% of cases, cells constrict after division of a neighboring cell (Figures 2D and 2G). Thus, in both cases, initiation of apical constriction correlates with a morphological reorganization of the embryo represented by a division event.

Please cite this article in press as: Samarage et al., Cortical Tension Allocates the First Inner Cells of the Mammalian Embryo, Developmental Cell (2015), http://dx.doi.org/10.1016/j.devcel.2015.07.004

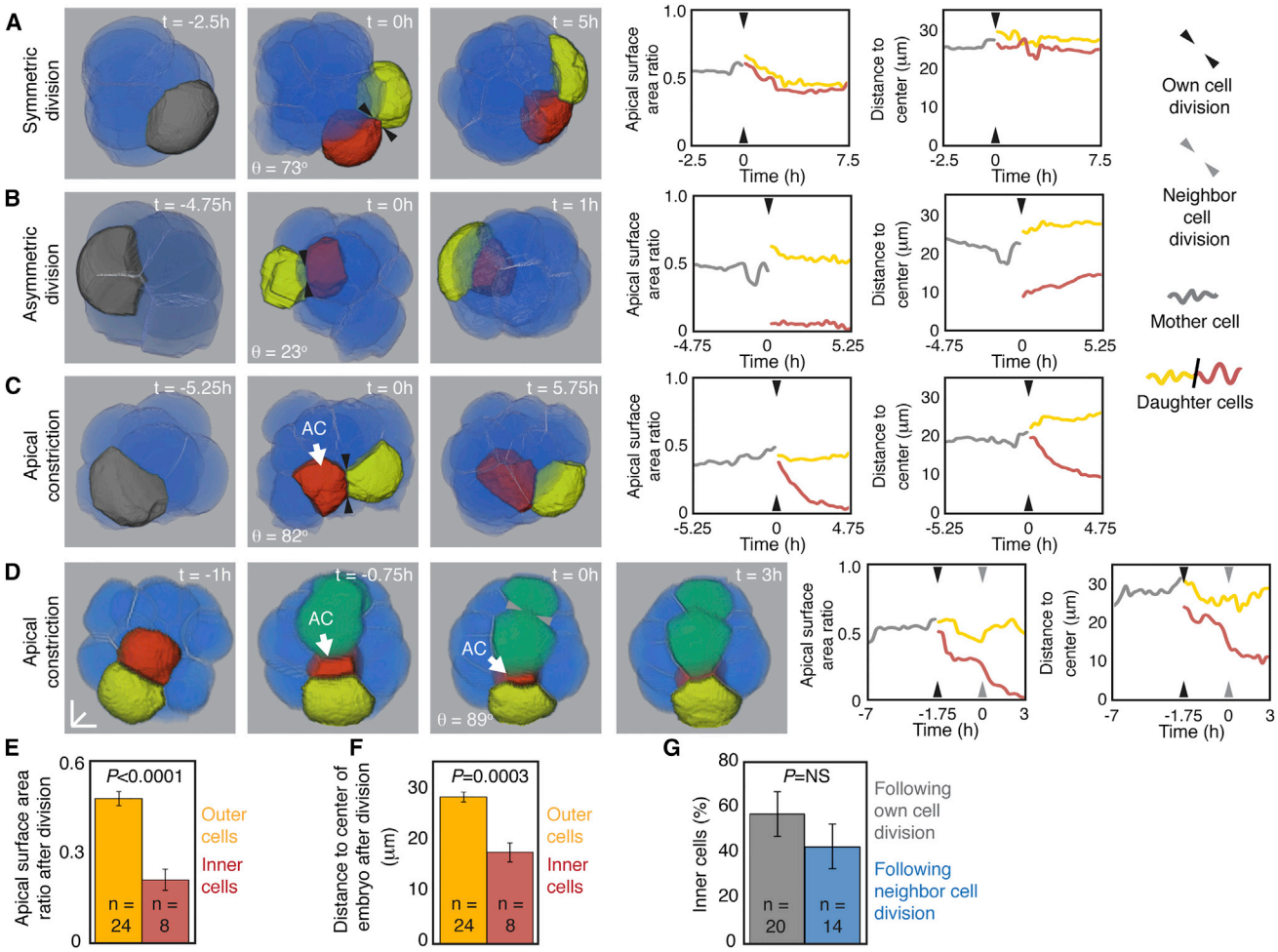

Figure 2. Changes in Surface Area and Position Identify Inner Cell Allocation via Apical Constriction

(A–D) Time frames of segmented living embryos show the distinct morphogenetic behaviors of cells following division. Computational segmentation of cell membranes allows quantitative tracking of the changes in cell surface area and position (distance from the center of the embryo). (A) Example of a parental cell (gray) undergoing symmetric division producing two daughter cells (red and yellow) that remain outside. (B) Example of a cell dividing asymmetrically, directly allocating one daughter inside the embryo as a result of the scission (red cell). (C) Example of a cell dividing symmetrically producing two outside cells. After dividing, one daughter cell (red cell) undergoes allocation inside the embryo by apical constriction (white arrow). (D) Example of a cell resulting from a symmetric division which undergoes apical constriction (red cell) following the division of a neighboring cell (green cell).

(E and F) Quantification of apical surface area and position of cells allocated outside the embryo or inside the embryo by apical constriction following their own division, as shown in (C).

(G) Quantification of cells undergoing apical constriction after their own division (as shown in C) or after division of a neighbor cell (as shown in D).

Arrowheads show division planes; θ is the division angle. Data are represented as mean ± SEM; p values were calculated by Student's t test. NS is not significant, and n represents number of cells tracked from 14 embryos. Scale bars represent 10 μm. See also Figures S1–S3.

We never observe two sister cells constricting simultaneously (n = 104 embryos).

Instead, cells constrict sequentially starting predominantly at the 12-cell stage (Figure 1G). While the constricting daughter becomes more cuboid, the daughter cell that remains outside adopts a wedge-like shape (Figure 1F). Our segmented embryos contain 2.9 ± 0.3 inner cells on average by the 16-cell stage (n = 33 embryos), in line with previous work (Kaur et al., 2013; Morris et al., 2010; Plachta et al., 2011). A similar proportion of cells is seen to undergo apical constriction using different membrane labeling approaches (Figures S2A–S2E). We also visualize bona fide apical constriction in non-injected embryos by differential interference contrast (DIC) microscopy (Figure S2F).

The founding cells internalized during the 8- to 16-cell stage are proposed to contribute more progeny to the fetus than those internalized later (Wennekamp et al., 2013; Yamanaka et al., 2006; Zernicka-Goetz et al., 2009). After the 16-cell stage, the embryo structure becomes more complex as the inner mass diverges into new lineages and the blastocoele forms. We tracked the first inner cells to show that they divide to expand the number of inner cells, while retaining their internal position (Figure S3). Additionally, new inner cells are contributed by asymmetric division of outer cells at a similar frequency to earlier stages and by apical constriction, albeit at a lower frequency. The more tightly packed architecture of the embryo (Johnson et al., 1986) may render apical constriction less favorable after the 16-cell stage.

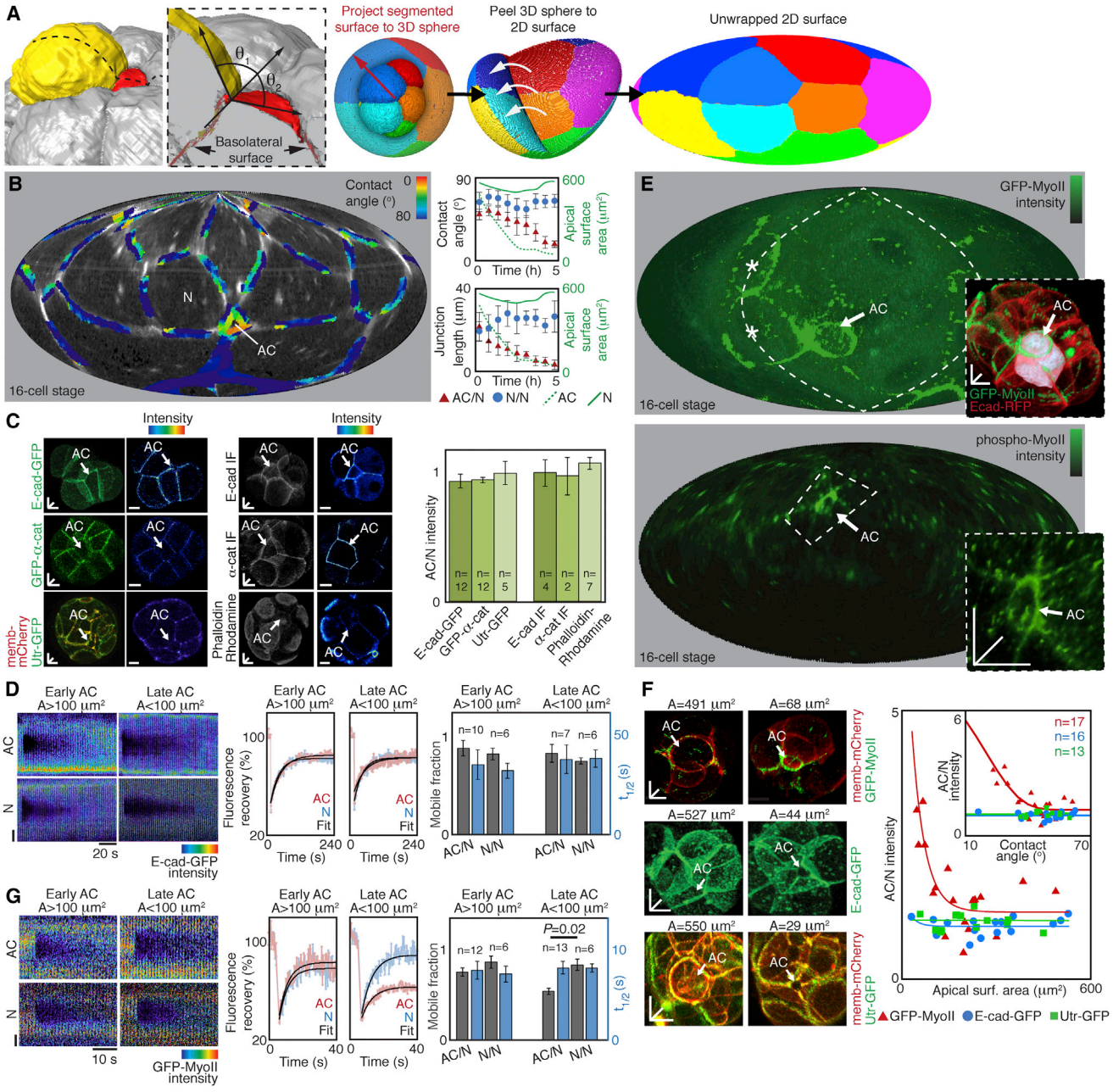

Figure 3. Apical Constriction Is Selectively Driven by Heterogeneities in Myosin II Distribution, but Not in E-Cadherin

(A) Schematic of method for measuring contact angles in 3D and generating computationally flattened 2D maps of whole living embryos.

(B) Contact angle distribution measured in 3D overlaid on flattened embryo map reveals narrower angles around constricting cells (AC). Graphs show mean contact angles and junction lengths between constricting cells and neighbors (AC/N) or neighbors alone (N/N) during apical constriction. Green lines show mean apical surface areas.

(C) Examples of E-cad-GFP, GFP-α-cat, and Utr-GFP distribution in live embryos and E-cadherin, α-catenin, and Phalloidin-Rhodamine (labeling F-actin) distribution in fixed embryos. All proteins and Phalloidin-Rhodamine show similar fluorescent intensities at junctions between constricting cells and adjacent neighbors. IF, immunofluorescence.

(D) FRAP kymographs (left) and quantitative analyses (middle and right) reveal similar E-cad-GFP mobility between constricting cells and their neighbors at different stages of apical constriction. Early and late apical constrictions (AC) are classified by measuring apical surface area (A).

(E) GFP-myosin II in living embryos (top view) and phospho-myosin II in fixed embryos (bottom view) accumulate around constricting cells. Asterisks show high GFP-myosin II levels also around a dividing neighbor cell. Dashed lines in 2D maps surround the 3D views in the inserts. Upper insert shows GFP-myosin II and E-cad-RFP expression in the live embryo.

(F) GFP-myosin II, E-cad-GFP, and Utr-GFP levels in constricting cells relative to their neighbors, as a function of apical surface area (A) and contact angle (inset). Only GFP-myosin II levels increase as cells constrict.

(legend continued on next page)

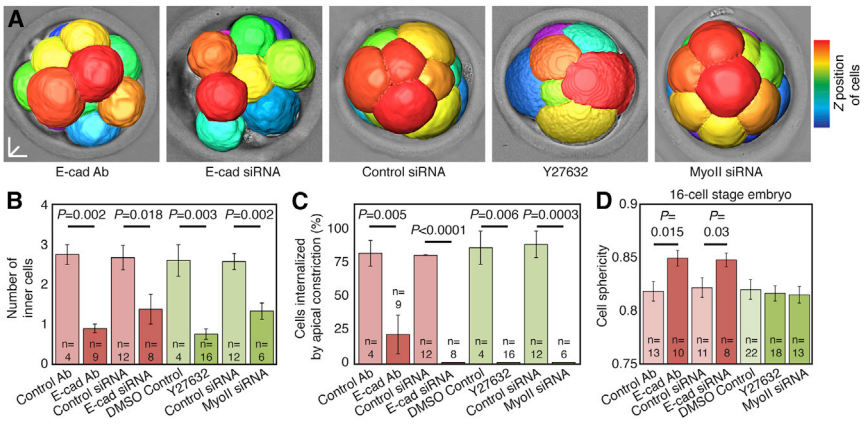

Figure 4. Effects of Disrupting E-Cadherin and Myosin II on Inner Cell Number, Apical Constriction, and Cell Sphericity

(A) Segmented live embryos after disrupting E-cadherin with an antibody or siRNAs, or myosin II with Y27632 or siRNAs.

(B and C) Disrupting E-cadherin and myosin II reduces inner cell numbers and inhibits apical constriction.

(D) Disrupting E-cadherin also affects cell sphericity, readily noticeable in the segmented embryos in (A).

Data are represented as mean ± SEM; p values by Student's t test. In (B) and (C), n represents number of embryos, and in (D), n represents number of cells from different embryos. All embryos were analyzed at 16-cell stage. Scale bars represent 10 μm. See also Figure S4.

Apical Constriction Is Selectively Driven by Heterogeneities in Cortical Tension, but Not in Cell Adhesion

Apical constriction underlies several morphogenetic processes (Martin and Goldstein, 2014). It is influenced by cell adhesion, typically mediated by cadherins, and cortical tension generated by the contractility of actomyosin networks. It remains a challenge to test how these biomechanical forces affect cell shape in mouse embryos. However, recent work shows that the influence of these forces can be investigated by measuring contact angles between cells. Recent studies correlated narrower contact angles with higher cortical tension (Krieg et al., 2008; Maître et al., 2012; Xiong et al., 2014). Thus, we developed a method to measure contact angles in 3D in segmented embryos (Figure 3A; Movie S3). Displaying these contact angles on computationally flattened whole-embryo maps shows that angles between constricting cells and their neighbors become narrower as apical constriction progresses (Figure 3B). Furthermore, the length of junctions formed between constricting cells and their neighbors decreases, whereas junctions between non-constricting neighbors remain similar (Figure 3B). This suggests that differences in cell adhesion or cortical tension may control inner cell allocation. Therefore, we determined how these morphological differences relate to the distribution of E-cadherin and myosin II in the living embryo.

E-cadherin fused to GFP (E-cad-GFP) accumulates at the basolateral regions of all cells (Figure 3C; Movie S4). Its levels, as well as those of its intracellular binding partner α-catenin fused to GFP (GFP-α-cat), are not significantly different between constricting cells and their neighbors and do not change during apical constriction (Figures 3C and 3F; Movie S4). Furthermore, fluorescence recovery after photobleaching (FRAP) experiments revealed no significant differences in E-cad-GFP mobility between cells at different stages of apical constriction (Figure 3D). Heterogeneities in contact angles are thus unlikely to arise from differences in E-cadherin-mediated adhesion between cells.

In contrast, myosin II distribution is heterogeneous and correlates with differences in contact angles (Figures 3B, 3E, and 3F). Both a GFP-myosin II fusion protein expressed in live embryos as well as endogenous phospho-myosin II in fixed embryos are enriched around constricting cells (Figures 3E and S4; Movie S5). Whereas the levels of F-actin visualized by Utrophin fused to GFP (Utr-GFP) are similar between cells and do not change as constricting cells reduce their apical surface area, those of GFP-myosin II increase with smaller areas (Figures 3C and 3F). Furthermore, unlike E-cad-GFP, FRAP experiments show that the GFP-myosin II mobile fraction decreases at more advanced apical constriction stages (Figure 3G).

Inner cell numbers and apical constriction are reduced after disrupting E-cadherin with a blocking antibody or siRNAs, or myosin II with siRNAs or the Rok inhibitor Y27632 shown to inhibit compaction and blastocoel formation in the mouse embryo (Duan et al., 2014; Laeno et al., 2013) (Figures 4 and S4). However, whereas interfering with myosin II does not noticeably disrupt embryo architecture, interfering with E-cadherin causes all cells to become more spherical (Figures 4A, 4D, and S4J). These results suggest that although E-cadherin is important to provide cell-cell coupling in the embryo, it does not have a more specialized function in determining which cells undergo apical constriction. Instead, progressive enrichment of myosin II around constricting cells suggests that cortical tension may play a more specific role in inner cell allocation. One possibility is that contractile forces act differently between cells of the embryo.

Subcellular Characterization of the Magnitude and Directionality of Tensile Forces

Technologies such as laser ablation or measurements of cell morphology have provided biomechanical insights into how forces control morphogenesis in non-mammalian organisms (Behrndt et al., 2012; Fernandez-Gonzalez et al., 2009; Kiehart et al., 2000; Krieg et al., 2008; Mayer et al., 2010; Rauzi et al.,

(G) FRAP experiments on GFP-MyoII show similar recovery time ($t_{1/2}$) for cells undergoing apical constriction at early and late stages but differences in the mobile fraction at later stages in AC cells in comparison to neighbors. The mobile fraction is significantly different at late AC stages between AC/N and N/N.

In (C), (D), (F), and (G), n represents number of cells from different embryos. Graphs in (B) were generated from four cells in different embryos. Data are represented as mean ± SEM; p values by Student's t test. Scale bars represent 10 μm in (C), (E), and (F) and 2 μm in (D) and (G). Color palettes show higher values in red. See also Figure S4.

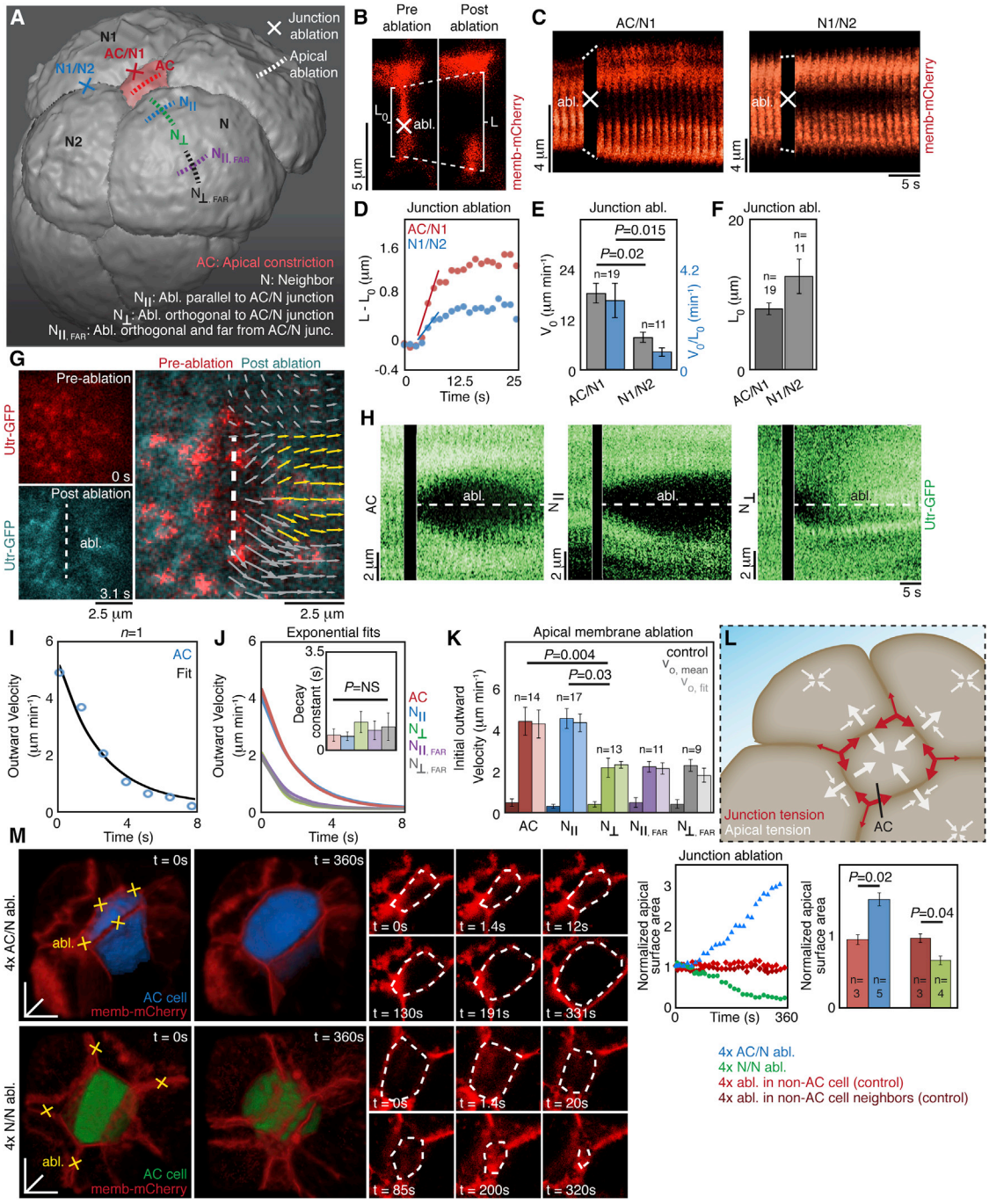

Figure 5. Subcellular Characterization of Tensile Forces Driving Inner Cell Mass Allocation

(A) Scheme of laser-ablated junctions and apical regions in living mouse embryos. A single femtosecond laser point was used for junction ablation. Six points along a line were used for apical ablations.

(B) Junction ablation example (abl., ablation).

(C) Junction ablation kymographs. Dashed lines highlight recoil response.

(D–F) Changes in junction length, V_0 and V_0 normalized by initial length (L_o) reveal that the junctions formed between constricting cells and their neighbors (AC/N1) have higher tension than neighbors alone (N1/N2).

(G) Example of PIV analysis of apical ablation. PIV analysis was applied to the entire image, but outward velocity was calculated by averaging the measurements at the sides of the cutting line, highlighted in yellow and shown on right side only.

(H) Apical ablation kymographs.

(I) Example of outward velocity as a function of time with exponential fit.

(J) Mean fits for all apical ablations. Inset shows similar decay constants.

(legend continued on next page)

2008; Xiong et al., 2014), but there have been no investigations in the early mouse embryo. Therefore, we established the use of laser ablation of actomyosin networks (Grill, 2011; Kiehart et al., 2000; Mayer et al., 2010; Rauzi and Lenne, 2011; Rauzi et al., 2008) in living mouse embryos. Targeting high laser energy into the cell cortex ablates local cortical organization and causes rapid recoil around the ablation. Measuring recoil speeds probes the directionality and relative magnitude of tensile forces acting at that region (Grill, 2011; Kiehart et al., 2000; Mayer et al., 2010; Rauzi and Lenne, 2011; Rauzi et al., 2008).

We first probed tensile forces along cell-cell junctions formed by cells undergoing apical constriction and their neighbors in live embryos expressing memb-mCherry (Figures 5A, 5B, and S6A–S6C). We used a femtosecond laser to target a subdiffraction limited volume at the apical part of the junction, where myosin II accumulates (Figure 3F). Ablation causes adjacent vertices to separate due to residual tensile forces. Membrane integrity is preserved and the ablated junction progressively recovers memb-mCherry (Figures S5A–S5C; Movie S6). We find that the maximal speed of separation V_0 is higher at junctions formed between a constricting cell and its neighbors (18.6 ± 2.7 μm min^{-1}) than between non-constricting neighbors (7.8 ± 1.2 μm min^{-1}), independent of junction length (Figures 5B–5F).

We next determined the tensile forces acting at the cell's apical cortex. We ablated multiple subdiffraction limited volumes along a 5 μm line in the cortical meshwork formed by F-actin, visualized by Utr-GFP. Applying particle image velocimetry (PIV) provides the speed of cortex movement orthogonal to the ablation (Figures 5A and 5G). Ablations performed in constricting cells cause rapid cortex displacement with a maximum outward velocity V_0 of 4.42 μm min^{-1}, followed by a slowing and recovery phase (Figures 5D–5F and S5D–S5G; Movie S7). Neighboring cells show similarly strong responses following ablation performed 3 μm away from the constricting cell and oriented parallel to the junction. However, significantly weaker reactions are obtained following ablations orthogonal to the junction (V_0 = 2.1 μm min^{-1}) or performed either parallel or orthogonal far from the junction in the central part of the neighbor's apical membrane (Figures 5H–5K). We did not find differences between the sister and other direct neighbors of the constricting cell, suggesting that all neighbor cells behave similarly (Figures S6A–S6C).

A schematic model summarizes the directionality and magnitude of tensile forces acting along junction and apical regions (Figure 5L). Together with the experiments showing higher myosin II levels around constricting cells (Figure 3), the findings indicate that an increase in cortical tension causes the apical surface of some cells to undergo constriction to be allocated inside the embryo.

The directionality and magnitude of tensile forces revealed by our laser ablation experiments suggest that forces acting along the constricting cell promote its internalization, while neighboring cells exert forces opposing the constriction process. In line with our model, simultaneous ablations performed along the middle point of four junctions of a constricting cell produce a rapid increase in surface area (Figure 5M, upper), whereas simultaneous ablations performed along four neighboring cell junctions produce the opposite effect. Immediately after ablation, the constricting cell decreases its surface area (Figure 5M, lower). Similar ablations at junctions of non-constricting cells or their neighbors do not cause marked changes in cell shape (Figures 5M and S6D). Time-lapse imaging reveals that after ablation the originally constricting cells resume their constriction and become internalized (Figure S6E).

Cortical Tension Is Required Not Only in Constricting Cells, but Also in Their Neighbors, for Cell Fate and Inner Cell Allocation

Next, we tested whether inhibiting apical constriction by blocking myosin II has consequences for cell fate in the embryo. Myosin II downregulation, whether in half of the embryo (Figure 6A) or in all cells (Figure 4B), reduces the number of inner cells to an average of one. Furthermore, blocking myosin II disrupts the normal pattern of cells expressing the transcription factors Cdx2 (Strumpf et al., 2005) and Sox2 (Avilion et al., 2003), markers associated with extraembryonic and pluripotent fate, respectively. These defects are detected not only in knockdown cells, but also in control (uninjected) cells of the same embryo (Figures 6B, 6C, and S7). These results suggest that the ability of control cells to constrict and provide the few inner cells found in these embryos depends on myosin II expression in their neighbors.

To explore the role of neighboring cells in inner cell allocation, we microinjected embryos at the one-cell stage with memb-mCherry, and then only one cell at the two-cell stage with myosin II siRNAs and H2B-GFP RNA, to visualize knockdown cells (Figure 7A). This experimental approach allows us to generate embryos with varying spatial configurations of knockdown and control cells, while avoiding the disruption of physiological mechanical forces likely to result from disaggregating and re-aggregating embryos. We found that control cells fail to constrict when they have three or more knockdown neighbors (Figures 7A–7E). Only when control cells have less than three knockdown neighbors do they successfully undergo apical constriction. Furthermore, the junctions between control cells and knockdown neighbors become significantly curved (Figure 7F), in line with local differences in cortical tension between these cells (Fujita and Onami, 2012). Therefore, although tensile forces in neighboring cells are lower in magnitude, their tension is still required for constricting cells to be allocated inside the embryo.

(K) Comparison of initial outward velocities obtained by PIV (V_{0mean}) and exponential fit (V_{0fit}) for different ablation regions and orientations.

(L) Schematic summary of tensile forces acting in constricting cells and their neighbors inferred from the junction and apical ablations.

(M) Simultaneous ablations performed at four junctions between a constricting cell and its neighbors (4× AC/N abl., upper panel) or between neighbors alone (4× N/N abl., lower). Large panels show 3D views pre-ablation and post-ablation. Smaller 2D planes show changes in apical perimeter (dashed lines). The constricting cell increases its surface area following 4× AC/N ablations and decreases its area following 4× N/N ablations. Graphs show example of changes in single-cell apical surface area over time (left) and mean changes in apical surface area at time 0 and 160 s.

Data are represented as mean ± SEM; n represents number of cells from different embryos. p values are determined by Student's t test; NS, not significant. Scale bars represent 10 μm. See also Figures S5 and S6.

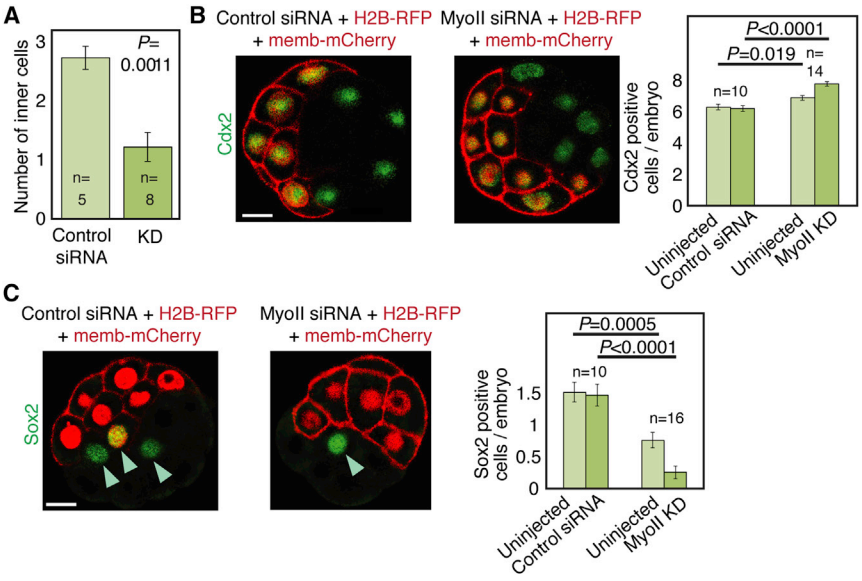

Figure 6. Myosin II Downregulation Perturbs Cell Fate

(A) Contribution of inner cells following injection of myosin II siRNAs (KD) or a scrambled control (control siRNA) and H2B-RFP and memb-mCherry RNA into one cell at the two-cell stage.

(B and C) Representative confocal Z-stacked sections show Cdx2 and Sox2 immunolabeling of microinjected embryos fixed at the 16-cell stage. More cells express Cdx2 and fewer cells express Sox2 in embryos microinjected with the myosin II siRNA compared with embryos injected with scrambled control. Cdx2 and Sox2 expression is similarly disrupted in the uninjected cells of the KD embryos. Arrowheads indicate inner cells in (C).

Data are represented as mean ± SEM; n represents number of embryos. p values are determined by Student's t test. Scale bars represent 10 μm. See also Figure S7.

DISCUSSION

We have discovered how tensile forces are organized in the developing mouse embryo and how they drive inner cell allocation. Our findings first confirm recent work suggesting that inner cells originate not only from asymmetric division, but also from internalization processes (Anani et al., 2014; McDole et al., 2011; Plusa et al., 2005; Watanabe et al., 2014; Yamanaka et al., 2010). Although recently a low-resolution membrane segmentation approach was applied to early mouse embryos, direct visualization of an internalizing cell was not provided (Watanabe et al., 2014). Furthermore, without quantitative descriptions, it remained unclear precisely what morphogenetic process underlies these internalization events and how frequently they occur. Here, we quantitatively describe the main changes in cell morphology and position as computationally reconstructed cells are allocated inside the embryo. The spatiotemporal changes we measured reveal that myosin II-dependent apical constriction, a key morphogenetic process shaping multicellular organisms (Martin and Goldstein, 2014), is responsible for spatially segregating cells during the very early stages of mammalian development. Furthermore, we show that asymmetric cell divisions, still assumed to form the inner mass in current models (Rossant and Tam, 2009; Wennekamp et al., 2013; Zernicka-Goetz et al., 2009), are not only uncommon, but even unnecessary during the initial formation of this structure, as during the 8- to 16-cell stage most embryos do not ever feature these divisions.

Membrane segmentation combined with computational flattening of live embryos revealed narrower cell-cell contact angles surrounding constricting cells. This indicates that as the embryo starts to produce its first inner cells, it develops differences in the balance of biomechanical forces. Previous work proposed that differences in cell adhesion contribute to sorting cells in mouse embryos (Kimber et al., 1982). This idea was broadly in line with the differential adhesion hypothesis (DAH), proposed to explain several morphogenetic processes (Fagotto, 2014; Steinberg, 2007). We find that in the mouse embryo, E-cadherin plays a role in coupling cells, in agreement with phenotypes observed in E-cadherin mutants (Stephenson et al., 2010). E-cadherin also resists the adoption of spheroidal cell shapes that, by Newton's kissing number calculation (Bender, 1874; Newton, 1846), would limit each inner mass to only one cell at the 16-cell stage. Our experiments disrupting E-cadherin confirm this single-cell inner mass, but importantly, we do not find differences between constricting cells and their neighbors in E-cadherin levels or mobility. Thus, heterogeneities in E-cadherin-mediated cell adhesion do not appear to play a more specialized role in determining which cells actually constrict. These results support concepts emerging from non-mammalian systems that differences in cortical tension play a more dedicated role than cell adhesion in several cell-sorting processes (Krieg et al., 2008; Lecuit et al., 2011; Maître et al., 2012; Rauzi and Lenne, 2011; Rauzi et al., 2008).

Unlike E-cadherin, myosin II accumulates specifically around constricting cells, and its mobile fraction decreases at more advanced stages of apical constriction. This agrees with a more selective role for cortical tension in determining which cells are allocated inside the embryo. Because apical constriction in the mouse embryo occurs on the timescale of hours, tensile forces would be at apparent equilibrium over shorter periods. However, laser ablations acutely disrupt the system, allowing measurements of tensile forces (Grill, 2011; Kiehart et al., 2000; Rauzi and Lenne, 2011; Rauzi et al., 2008). We demonstrate that tensile forces are higher in magnitude at junctions formed between constricting cells and their neighbors than between neighbors alone. This suggests that circumferential contractile networks are the main drivers of apical constriction in the mouse embryo. Such spatial organization of forces correlates with the enrichment of myosin II along cell junctions, rather than formation of the large medioapical contractile foci found in other systems (Martin and Goldstein, 2014). We also verified our proposed model of how tensile forces act in the embryo (Figure 5L) using acute perturbations of apical constriction. Perturbing the forces acting around constricting cell junctions negatively

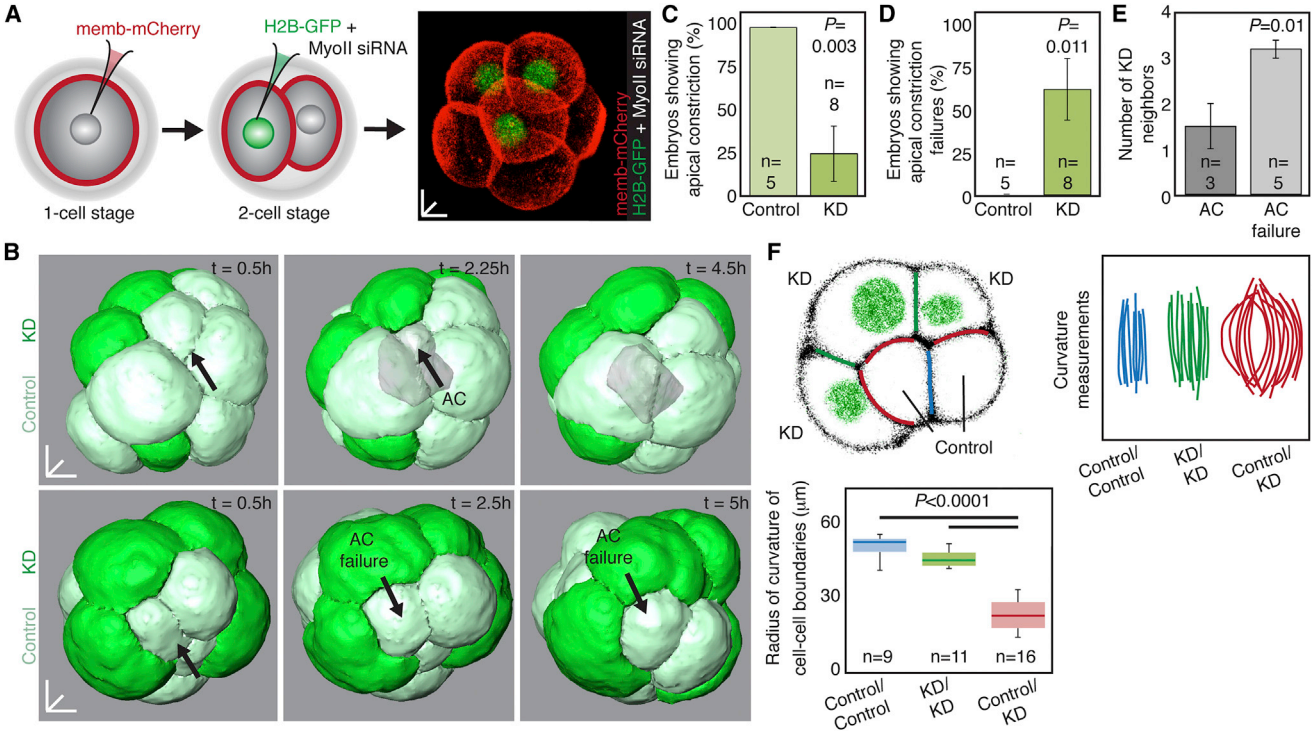

Figure 7. Apical Constriction Requires Cortical Tension in Neighboring Cells

(A) Experimental design for tracking all cells in the embryo when myosin II is downregulated in only half of the cells. H2B-GFP expression identifies KD cells.

(B) Segmented embryos microinjected as described in (A). Selected time frames show control cells (arrows) undergoing normal apical constriction (AC, upper) or featuring signs of apical constriction failure (lower).

(C) Percentage of embryos showing apical constriction.

(D) Percentage of embryos showing signs of apical constriction failure.

(E) Relationship between apical constriction failure and number of KD neighboring cells. Apical constriction of control cells fails when they have three KD neighbors.

(F) Single plane of living embryo features curved junctions between control and KD cells (left). Defects in membrane curvature are revealed by tracing junctions and calculating junction curvature.

Data are represented as mean ± SEM. In (C) and (D), n represents number of embryos; in (E), n represents number of cells from eight embryos, and in (F), n represents number of boundaries from 8 embryos. p values are determined by Student's t test; scale bars represent 10 μm.

impacts the constriction process, whereas ablations performed on neighboring junctions facilitate the reduction in apical surface area (Figure 5M).

The laser ablations of actomyosin networks demonstrate the subcellular distribution of the tensile forces acting in vivo (Figure 5L). In the apical membrane of the constricting cell, tensile forces are high and isotropic. In contrast, in neighboring cells these forces are high and anisotropic in the regions adjacent to the constricting cell, but are lower and isotropic far from the constricting cell. These local anisotropies in tension forces may originate from a combination of geometrical changes caused by constricting cells exerting a pulling effect on their neighbors as shown in other systems (Kiehart et al., 2000), as well as the induction of cortical flows in the latter (Mayer et al., 2010). The attenuation of tensile forces with distance away from the constricting cell indicates that neighboring cell cortices behave as viscoelastic networks, where cortical tension dissipates, preventing the long-range propagation of contractile forces. We propose that unlike in more cohesive tissues (Fernandez-Gonzalez et al., 2009; Kiehart et al., 2000; Rauzi et al., 2008), such a "force buffering" effect by neighboring cells enables confined internalization of a constricting cell without globally jeopardizing embryo architecture.

By downregulating myosin II in only half of the cells of the embryo, we found that cortical tension is required not only in constricting cells, but also in their neighbors for normal inner cell allocation. Cortical tension in neighboring cells may provide the substrate for force transmission necessary for constricting cells to coordinate their own changes in shape. This idea is supported by the observation that when myosin II is downregulated in neighboring cells constricting cells adopt abnormal shapes, protruding outward against a neighboring structure, which likely offers reduced resistance. When fewer cells are internalized due to myosin II downregulation, the cells that remain outside express Cdx2 and the fewer cells that internalize express Sox2. Therefore, cells regulate Cdx2 and Sox2 expression according to their position in the embryo and are unlikely predetermined to express these markers in a context-independent manner.

Although it remains debated whether inner cells originate from deterministic events or random cell interactions (Rossant and Tam, 2009; Wennekamp et al., 2013; Zernicka-Goetz et al., 2009), our findings show that apical constriction can arise either

immediately following division of the parental cell or after cell-repositioning events associated with division of neighboring cells. Cells in the embryo do not always display the same pattern of internalization to form the inner mass. However, we find that the first cell undergoes apical constriction predominantly at the 12-cell stage. This suggests that cells divide stochastically to reach a threshold number, at which point physical constraints mean a cell must internalize, without determining which one.

It will be interesting to reveal how heterogeneities in myosin II distribution and tensile forces originate. These events may be linked to signaling pathways regulating cell fate during mammalian development such as Hippo signaling, transcription factor dynamics, or epigenetic changes (Jedrusik et al., 2008; Kaur et al., 2013; Morris et al., 2010; Plachta et al., 2011; Porazinski et al., 2015; Torres-Padilla et al., 2007). However, they may also arise from mechanosensor responses of myosin II proposed in other processes (Fernandez-Gonzalez et al., 2009; Kim et al., 2015). Finally, our study also introduces a new system to investigate how apical constriction, a key morphogenetic process controlling embryogenesis and tissue formation, is regulated in vivo and in mammals.

EXPERIMENTAL PROCEDURES

DNA and RNA Work

The E-cad-GFP and memb-mCherry constructs were described previously (Fierro-González et al., 2013). The sequence for human nonmuscle myosin IIA (Addgene: 11347) was cloned downstream of GFP in a pCS2 vector. RNA transcription and purification were performed using pCS2 vectors and the mMESSAGE mMACHINE SP6 kit (Ambion) and RNAeasy kit (QIAGEN) following manufacturer's instructions. RNA for memb-mCherry was injected at 30 ng/μl, E-cad-GFP, and GFP-Myosin II at 50 ng/μl and Utr-GFP and GFP-α-cat at 75 ng/μl. siRNAs (QIAGEN) for Scrambled (Ctrl_Allstars_1) E-cad (Mm_Cdh1_5, Mm_Cdh1_6) or Myosin II (Mm_Myh9_1, Mm_Myh9_3) were microinjected at a final concentration of 200 nM. The sequences of the siRNAs used were Ctrl_Allstars_1 (undisclosed by QIAGEN), Mm_Cdh1_5 (ACGGAGGAGAACGGTGGTCAA), Mm_Cdh1_6 (CCGGGACAATGTGTATTACTA), Mm_Myh9_1 (CAGGGCTTATCTACACCTATT), and Mm_Myh9_3 (TCCAGCAAGAATGGCTTTGAA).

The efficiency of the E-cad siRNA has been previously demonstrated (Fierro-González et al., 2013). For the E-cad rescue experiments E-cad-GFP or E-cad-ΔICD-GFP were injected at 30 ng/μl with the Cdh1_5 siRNA, which targets the 3′ UTR of E-cadherin. For the myosin II rescue experiments, GFP-Myosin II RNA was microinjected at 50 ng/μl with the Mm_Myh9_3 siRNA, which targets the 5′ UTR of Myosin II. Microinjection of RNA for E-cad-GFP, GFP-Myosin II, Utr-GFP, and GFP-α-cat did not interfere with normal development to blastocyst stage.

Mouse Embryo Work

Experiments were performed following Monash University Animal Ethics guidelines. We used superovulated C57BL/6, B6CBA-F1, and B6CBA-SWISS WTe females or a transgenic strain expressing GFP fused to a membrane localization signal (Fierro-González et al., 2013) driven from the CAG promoter (containing the chicken beta-actin promoter, minimum cytomegalovirus enhancer, and a large synthetic intron) in a C57BL/6 background at 28–32 days of age. We obtained no significant differences in the extent of apical constriction or number of inner cells at the 8- to 16-cell stage between mice of different strains. Mice were euthanized by cervical dislocation and embryos flushed from oviducts with M2 medium (Merck) and cultured in KSOM+AA (Merck) at 37°C and 5% CO_2 covered by mineral oil (Sigma). Between 0.1 and 0.3 pL RNA diluted in injection buffer (5 mM Tris, 5 mM NaCl, 0.1 mM EDTA) was microinjected with a FemtoJet (Eppendorf). For imaging, embryos were cultured in LabTek chambers (Nunc) at 37°C and 5% CO_2 in an incubator adapted for the microscope system (Zeiss, Jena). For immunolabeling, embryos were fixed in 4% paraformaldehyde in Dulbecco's phosphate-buffered saline (DPBS) for 30 min, washed in DPBS containing 0.1% Triton X-100, permeabilized for 30 min in DPBS containing 0.25% Triton X-100, incubated in blocking solution (10% fetal bovine serum in DPBS) for 2 hr, incubated with antibodies for phospho-myosin IIa (3671P, Cell Signaling) at 1:200, myosin IIa (3403, Cell Signaling) at 1:100, Cdx2 (88129, Abcam) at 1:250, Sox2 (ab59776, Abcam) at 1:250, anti-E-cad DECMA-1 (Sigma, U3254) at 1:100, anti-α-cat (Sigma C2081) at 1:2,000 in blocking solution overnight at 4°C, rinsed in DPBS, incubated with goat anti-rabbit-488 secondary (Invitrogen) in blocking solution (1:500) for 2 hr, and rinsed in DPBS. To label F-actin, fixed embryos were incubated with Phalloidin-Rhodamine (Molecular Probes, R415) at 1:500. For E-cad function blocking, we treated eight-cell stage embryos with the DECMA-1 antibody (1:1,500, Sigma U3254) or control IgG antibody at the same concentration in KSOM+AA. For Myosin II inhibition, we treated eight-cell stage embryos with Y27632 at 100 μM and controls with DMSO at 1:1,000 in KSOM+AA. To quantify immunofluorescence, we measured mean fluorescence intensity along the entire length of a cell-cell junction and normalized by the area measured.

Live Embryo Imaging

Live embryos were imaged using a Zeiss LSM 780 microscope (Zeiss, Jena). For two-photon imaging, we used a reflected light BiG GaAsP NDD module and a multiphoton Ti:Sapphire laser (Chameleon, Coherent) set to ~3% transmission. We collected emitted light with appropriate filters, with 1 μm intervals along the z axis. For confocal imaging we used avalanche photodiodes of the Confocor 3 module (Zeiss, Jena). Fusion proteins were imaged with 488 nm light for GFP and with 561 nm light for mCherry with appropriate filter combinations. DIC was performed using appropriate prisms. A water-immersion C-Apochromat 40×/1.2 NA objective was used for all experiments except for the laser ablations. Our imaging conditions allow development of over 80% of embryos to blastocyst stage, similar to non-injected and non-imaged embryos. The remaining 20% of embryos showing signs of abnormal or arrested development were excluded following established criteria (Fierro-González et al., 2013; Kaur et al., 2013; Morris et al., 2010). We previously demonstrated that embryos microinjected and imaged with similar conditions can generate viable offspring following transfer to pseudopregnant mice (Kaur et al., 2013). For experiments determining inner cell number at the 16-cell stage, cells were counted at the last time-point at which the embryo contained 16-cells, before 1 cell divided to produce a 17-cell embryo.

Cell Segmentation and 4D Tracking

We used the 3D and 4D imaging data of embryos expressing memb-mCherry or E-cad-GFP for cell segmentation. The membrane data stack corresponded to a region of interest of 106 × 106 × 89 μm (lateral resolution 0.208 μm $pixel^{-1}$, axial resolution 1 μm $pixel^{-1}$). Using custom software, the membrane label stacks were binned using a Hermite interpolation filter and interpolated axially using cubic spline interpolation scheme, to obtain a data stack with equal lateral and axial resolutions of 0.416 μm/pixel. A median filter (three-pixels window size) was applied to the data stacks for minor noise reduction. A fissure enhancement approach (Shamonin et al., 2012; Lassen et al., 2013) was used in conjunction with Gaussian smoothing to enhance the membrane data within the data stack. This fissure enhancement technique rates the strength of membrane structure within the image and reduces noise. The filtered membrane data were used to prepare the cost image for watershed segmentation using FEI Avizo 8 (Visualization Sciences Group) software. The membrane was segmented out of the filtered data by thresholding, and an image closing technique was used to close any gap in the segmented membrane data. A distance transform was applied to the binary membrane data (segmented) and inverted. The brightest (maxima) pixels within this map were used to estimate the position of the cell centers. Watershed segmentation was applied to the segmented membrane data using the cell center data as markers to segment the cells from the membrane data stack. This process was repeated for multiple time points in the acquired 4D data stack of the living embryo. The cells were tracked based on the volume occupied within the image with properties such as cell volume, surface area, apical surface area, position of the cell center of mass (COM), and COM of the entire embryo recorded at each time point. The software was designed to search for a cell's COM within the volume occupied by the tracked cell in the previous time point.

If there exists two COM's within this volume, the cell was understood to have divided. We did not encounter more than two COMs at any given moment during the analysis. If a cell has divided, the orientation of cell division is determined by the angle between the line connecting the COMs of the two sister cells (line S_1S_2) and the line connecting the COM of the embryo (O) to the midpoint of line S_1S_2 (M). See Figures 1 and S1C for a schematic of the angle of divisions. The range between 0 and 90 degrees was divided equally into the three traditional categories of symmetric, oblique, and asymmetric divisions. Division angles between 0 and 30 degrees were classified as asymmetric, and the remaining divisions were pooled into a single symmetric classification, as they result in daughter cells with varying amounts of membrane exposed to the zona pellucida.

Other quantitative measures such as cell volume and cell surface are readily available. We quantified both the total surface area of any given cell, A_{total}, as well as the apical surface area, A_{apical} of the cell using custom software. We plotted the apical surface area ratio, which we define as the ratio between the apical surface area and the total cell surface area to classify between the different cell division behaviors. In addition to apical surface area ratio, we quantified the distance between the cell COM and the embryo COM (Figure 2).

Analyses of Level and Distribution of Proteins and Transcripts

Expression levels of E-cad-GFP, GFP-α-cat, Utr-GFP, and GFP-Myosin II were quantified by measuring fluorescence intensity and normalizing to memb-mCherry within the same cell using ImageJ. A red-to-blue color palette was used to illustrate high-to-low intensity in displayed images. Total mRNA was extracted using the Arcturus PicoPureAR RNA Isolation Kit (Applied Biosystems) in combination with the RNase-Free DNase Set (QIAGEN) according to manufacturer's instructions. qRT-PCR was performed using the TaqManAR RNA-to-CT 1-Step Kit (Applied Biosystems) and an Mx3000P QPCR system (Stratagene). Quantification was performed using the comparative Ct method with normalization to beta-actin. Primers were as follows: MyoIIA (F) GAAGAA GGTGAAGGTGAACAAGG, (R) TCTGTGATGGCGTAGATGTGG, and beta-actin (F) GTCCACACCCGCCACCAG, (R) TGACCCATTCCCACCATCAC.

Contact Angle Measurement

Contact angles were calculated at cell-cell junctions of the 3D segmented embryo. The contact angle is measured between the apical surface and cell-cell basolateral surface (Figure 3A). The line of intersection between two cells and the basolateral surface was determined by applying a spline interpolation to the set of points along the junction, which have been ordered through solving a traveling salesman problem. Angles were measured at multiple points along the junction. Two surfaces defined by a second order polynomial were fitted to neighboring points along the apical and basolateral surfaces, allowing calculation of the angle between the cells.

Projection to a 2D Surface

The apical surface area of the embryo exposed to the zona pellucida was projected onto a sphere by ray casting from the center of mass of the embryo. An equal-area map projection known as the Hammer projection was applied to the sphere to obtain the 2D projected map of the apical surface.

FRAP

FRAP experiments were performed with a Zeiss C-Apochromat 40×/1.20 objective at 7× zoom magnification. A 4 × 4 μm region of interest (ROI) was photobleached with 100% 488 nm laser power. Mean ROI fluorescence intensity was corrected by background fluorescence and normalized to the mean intensity ratio between pre-photobleaching and post-photobleaching from a non-bleached membrane region. The pre-bleaching intensity value was taken as 100%. Normalized fluorescence intensity I(t) data were fitted with a single exponential function:

$$I(t) = I(0) + (I_\infty - I(0))\left(1 - e^{-\frac{t}{\tau}}\right),$$

where I(0) is the fluorescence intensity immediately after bleaching, I_∞ is the fluorescence intensity when the intensity reaches a plateau, and τ is the characteristic time. The mobile fraction was calculated as $I_\infty - I(0)/1 - I(0)$ and the half time as $\tau \ln(2)$.

Cell Shape Analysis

The Wadell sphericity index (Wadell, 1932) was used to define cell sphericity:

$$\text{Cell sphericity} = \frac{\pi^{1/3}(6Vol)^{2/3}}{A_{total}},$$

where Vol is the cell volume and A_{total} is the total surface area of the cell as calculated by our custom software.

To determine the curvature of cells (Figure 7F), cell junctions were traced as ROIs, and circles were fit to each ROI with ImageJ. The curvature of the cell-cell boundary was determined by the radius of the fitted circle.

Laser Ablations

Laser ablations were performed using a Zeiss oil immersion 63×/1.4 NA objective and a multiphoton Ti:Sapphire laser (Chameleon, Coherent) tuned to 790 nm and set to 50% maximal power. Before and after ablation of either junctions or apical membranes, 4 μm thick confocal images were acquired at 5× magnification using avalanche photodiodes every 1.3 s. For junction ablations, we used embryos expressing memb-mCherry imaged with 561 nm light. A 0.5 μm radius circular spot was scanned at 1 μs pixel^{-1} at the middle point of the apical region of the cell-cell junction. The maximal speed of displacement reflects tension at the targeted junction before ablation (Rauzi and Lenne, 2011). Vertex distance was measured with ImageJ. Maximal velocity was obtained from the slope of a linear fitting of the displacement for the first 5 s after ablation. We only performed laser ablations on cell junctions positioned directly in front of the imaging objective extending exclusively along the lateral axis. This ensures that following ablation the recoil occurs almost exclusively along lateral directions. Junctions extending along the z axis were excluded from these experiments.

For ablation of the apical membrane we adapted techniques previously used in other systems (Mayer et al., 2010). Six equidistant 0.5 μm radius circular spots were scanned at 1 μs pixel^{-1} along a 5 μm line of the apical cortex in embryos expressing Utr-GFP. We quantified field velocity for pre-ablation and post-ablation images using PIV (Samarage et al., 2012). The velocity component orthogonal to the ablation line was averaged in a 5 × 3 μm region to obtain V_{0mean}. Control velocity measurements were obtained with the same approach from the pre-ablation image. We calculated the velocity for each time interval and obtained V_{0fit} by exponential fitting. Decay constants were not significantly different between different ablation regions, indicating homogenous cortex stiffness (Mayer et al., 2010). For the junction ablations, we monitored normal membrane integrity by the progressive recovery of memb-mCherry labeling along the ablated junction or Utr-GFP at the apical cell cortex, which were evident 10–30 s after ablation. We also assessed that after ablation some of these cells (n = 10) undergo apical constriction and can be found in the inner region of the embryo following the 16-cell stage, indicating that cell integrity is maintained. We excluded from analysis cells damaged after ablation, which represented 22% of the cases. In these cells, the ablation produced a large tearing of the plasma membrane visible by DIC immediately after ablation, with obvious spilling of cytoplasmic material. For Figure 5M, four junction laser ablations were performed at the same time and the region around the ablated cell was tracked in 4D by time-lapse confocal microscopy using APDs for detection. We verified that these ablated embryos continue to develop following the 4× junction ablation protocol. Embryos showing signs of photodamage due to mistargeting of the laser were readily noticeable and excluded from analysis.

Live Identification of Apical Constriction

For the laser ablation experiments, we identified cells undergoing apical constriction by their characteristic change in morphology compared with their neighbors. In line with our segmentation results (Figure 1), constricting cells progressively shrink their apical membrane. Their apical borders become more rectangular, and they adopt a cuboid 3D shape. Ablations were performed when constricting cells had shrunk their apical surface by 50% to 70% of their original area. We tracked some of these cells in 4D to confirm they complete internalization and integrate in the internal region of the embryo (n = 10/10 tracked cells).

PIV Analysis

Instantaneous PIV measurements were made using custom in-house software (Samarage et al., 2012).

Statistical Analyses

Statistical analyses were performed with GraphPad Prism and MATLAB software. Unpaired, two-tailed Student's t test was used, with data represented as mean ± SEM. For strength of p value estimates, we always assumed unequal variances. The experiments were not randomized, and no statistical method was used to predetermine sample size. Reproducibility of all results was confirmed by independent experiments. All experiments were repeated a minimum of three times.

SUPPLEMENTAL INFORMATION

Supplemental Information includes Supplemental Experimental Procedures, seven figures, and seven movies and can be found with this article online at http://dx.doi.org/10.1016/j.devcel.2015.07.004.

AUTHOR CONTRIBUTIONS

All authors designed and performed experiments and helped write the manuscript.

ACKNOWLEDGMENTS

We thank Juan Silva for help with mouse microinjections, Toby Bell for laser ablations, and Mate Biro and Alpha Yap for comments on the manuscript. This work was supported by the Multi-modal Australian ScienceS Imaging and Visualisation Environment (MASSIVE) (http://www.massive.org.au), the Australian Research Council (DP120104594 and DE120100794 to N.P.), National Health and Medical Research Council (APP1022721 to A.F. and APP1052171 and APP1062263 to N.P.), Viertel Foundation Medical Research Fellowship (to N.P.), Monash University Strategic Grant (to A.F. and N.P.), UK Medical Research Council (G0802057 to E.C.J) and Wenner-Gren Foundations and Swedish Society for Medical Research (to J.C.F.-G.), and A*STAR Investigatorship 1430700132 (N.P.).

Received: March 23, 2015
Revised: May 18, 2015
Accepted: July 13, 2015
Published: August 13, 2015

REFERENCES

Anani, S., Bhat, S., Honma-Yamanaka, N., Krawchuk, D., and Yamanaka, Y. (2014). Initiation of Hippo signaling is linked to polarity rather than to cell position in the pre-implantation mouse embryo. Development *141*, 2813–2824.

Avilion, A.A., Nicolis, S.K., Pevny, L.H., Perez, L., Vivian, N., and Lovell-Badge, R. (2003). Multipotent cell lineages in early mouse development depend on SOX2 function. Genes Dev. *17*, 126–140.

Behrndt, M., Salbreux, G., Campinho, P., Hauschild, R., Oswald, F., Roensch, J., Grill, S.W., and Heisenberg, C.P. (2012). Forces driving epithelial spreading in zebrafish gastrulation. Science *338*, 257–260.

Bender, C. (1874). Bestimmung der grössten Anzahl gleich Kugeln, welche sich auf eine Kugel von demselben Radius, wie die übrigen, auflegen lassen. Archiv. Math. Physik (Grunert) *56*, 302–306.

Dard, N., Louvet-Vallée, S., and Maro, B. (2009). Orientation of mitotic spindles during the 8- to 16-cell stage transition in mouse embryos. PLoS ONE *4*, e8171.

Duan, X., Chen, K.L., Zhang, Y., Cui, X.S., Kim, N.H., and Sun, S.C. (2014). ROCK inhibition prevents early mouse embryo development. Histochem. Cell Biol. *142*, 227–233.

Fagotto, F. (2014). The cellular basis of tissue separation. Development *141*, 3303–3318.

Fernandez-Gonzalez, R., Simoes, Sde.M., Röper, J.C., Eaton, S., and Zallen, J.A. (2009). Myosin II dynamics are regulated by tension in intercalating cells. Dev. Cell *17*, 736–743.

Fierro-González, J.C., White, M.D., Silva, J.C., and Plachta, N. (2013). Cadherin-dependent filopodia control preimplantation embryo compaction. Nat. Cell Biol. *15*, 1424–1433.

Fujita, M., and Onami, S. (2012). Cell-to-cell heterogeneity in cortical tension specifies curvature of contact surfaces in Caenorhabditis elegans embryos. PLoS ONE *7*, e30224.

Gelbart, M.A., He, B., Martin, A.C., Thiberge, S.Y., Wieschaus, E.F., and Kaschube, M. (2012). Volume conservation principle involved in cell lengthening and nucleus movement during tissue morphogenesis. Proc. Natl. Acad. Sci. USA *109*, 19298–19303.

Grill, S.W. (2011). Growing up is stressful: biophysical laws of morphogenesis. Curr. Opin. Genet. Dev. *21*, 647–652.

Heisenberg, C.P., and Bellaïche, Y. (2013). Forces in tissue morphogenesis and patterning. Cell *153*, 948–962.

Jedrusik, A., Parfitt, D.E., Guo, G., Skamagki, M., Grabarek, J.B., Johnson, M.H., Robson, P., and Zernicka-Goetz, M. (2008). Role of Cdx2 and cell polarity in cell allocation and specification of trophectoderm and inner cell mass in the mouse embryo. Genes Dev. *22*, 2692–2706.

Johnson, M.H., and Ziomek, C.A. (1981). The foundation of two distinct cell lineages within the mouse morula. Cell *24*, 71–80.

Johnson, M.H., Maro, B., and Takeichi, M. (1986). The role of cell adhesion in the synchronization and orientation of polarization in 8-cell mouse blastomeres. J. Embryol. Exp. Morphol. *93*, 239–255.

Kaur, G., Costa, M.W., Nefzger, C.M., Silva, J., Fierro-González, J.C., Polo, J.M., Bell, T.D., and Plachta, N. (2013). Probing transcription factor diffusion dynamics in the living mammalian embryo with photoactivatable fluorescence correlation spectroscopy. Nat. Commun. *4*, 1637.

Kiehart, D.P., Galbraith, C.G., Edwards, K.A., Rickoll, W.L., and Montague, R.A. (2000). Multiple forces contribute to cell sheet morphogenesis for dorsal closure in Drosophila. J. Cell Biol. *149*, 471–490.

Kim, J.H., Ren, Y., Ng, W.P., Li, S., Son, S., Kee, Y.S., Zhang, S., Zhang, G., Fletcher, D.A., Robinson, D.N., and Chen, E.H. (2015). Mechanical tension drives cell membrane fusion. Dev. Cell *32*, 561–573.

Kimber, S.J., Surani, M.A., and Barton, S.C. (1982). Interactions of blastomeres suggest changes in cell surface adhesiveness during the formation of inner cell mass and trophectoderm in the preimplantation mouse embryo. J. Embryol. Exp. Morphol. *70*, 133–152.

Krieg, M., Arboleda-Estudillo, Y., Puech, P.H., Käfer, J., Graner, F., Müller, D.J., and Heisenberg, C.P. (2008). Tensile forces govern germ-layer organization in zebrafish. Nat. Cell Biol. *10*, 429–436.

Laeno, A.M., Tamashiro, D.A., and Alarcon, V.B. (2013). Rho-associated kinase activity is required for proper morphogenesis of the inner cell mass in the mouse blastocyst. Biol. Reprod. *89*, 122.

Lassen, B., van Rikxoort, E.M., Schmidt, M., Kerkstra, S., van Ginneken, B., and Kuhnigk, J.M. (2013). Automatic segmentation of the pulmonary lobes from chest CT scans based on fissures, vessels, and bronchi. IEEE Trans. Med. Imaging *32*, 210–222.

Lecuit, T., and Lenne, P.F. (2007). Cell surface mechanics and the control of cell shape, tissue patterns and morphogenesis. Nat. Rev. Mol. Cell Biol. *8*, 633–644.

Lecuit, T., Lenne, P.F., and Munro, E. (2011). Force generation, transmission, and integration during cell and tissue morphogenesis. Annu. Rev. Cell Dev. Biol. *27*, 157–184.

Maître, J.L., Berthoumieux, H., Krens, S.F., Salbreux, G., Jülicher, F., Paluch, E., and Heisenberg, C.P. (2012). Adhesion functions in cell sorting by mechanically coupling the cortices of adhering cells. Science *338*, 253–256.

Martin, A.C., and Goldstein, B. (2014). Apical constriction: themes and variations on a cellular mechanism driving morphogenesis. Development *141*, 1987–1998.

Mayer, M., Depken, M., Bois, J.S., Jülicher, F., and Grill, S.W. (2010). Anisotropies in cortical tension reveal the physical basis of polarizing cortical flows. Nature *467*, 617–621.

McDole, K., Xiong, Y., Iglesias, P.A., and Zheng, Y. (2011). Lineage mapping the pre-implantation mouse embryo by two-photon microscopy, new insights into the segregation of cell fates. Dev. Biol. *355*, 239–249.

Morris, S.A., Teo, R.T., Li, H., Robson, P., Glover, D.M., and Zernicka-Goetz, M. (2010). Origin and formation of the first two distinct cell types of the inner cell mass in the mouse embryo. Proc. Natl. Acad. Sci. USA *107*, 6364–6369.

Newton, I. (1846). Mathematical Principles of Natural Philosophy (New York: Daniel Adee).

Plachta, N., Bollenbach, T., Pease, S., Fraser, S.E., and Pantazis, P. (2011). Oct4 kinetics predict cell lineage patterning in the early mammalian embryo. Nat. Cell Biol. *13*, 117–123.

Plusa, B., Frankenberg, S., Chalmers, A., Hadjantonakis, A.K., Moore, C.A., Papalopulu, N., Papaioannou, V.E., Glover, D.M., and Zernicka-Goetz, M. (2005). Downregulation of Par3 and aPKC function directs cells towards the ICM in the preimplantation mouse embryo. J. Cell Sci. *118*, 505–515.

Porazinski, S., Wang, H., Asaoka, Y., Behrndt, M., Miyamoto, T., Morita, H., Hata, S., Sasaki, T., Krens, S.F., Osada, Y., et al. (2015). YAP is essential for tissue tension to ensure vertebrate 3D body shape. Nature *521*, 217–221.

Rauzi, M., and Lenne, P.F. (2011). Cortical forces in cell shape changes and tissue morphogenesis. Curr. Top. Dev. Biol. *95*, 93–144.

Rauzi, M., Verant, P., Lecuit, T., and Lenne, P.F. (2008). Nature and anisotropy of cortical forces orienting Drosophila tissue morphogenesis. Nat. Cell Biol. *10*, 1401–1410.

Rossant, J., and Tam, P.P. (2009). Blastocyst lineage formation, early embryonic asymmetries and axis patterning in the mouse. Development *136*, 701–713.

Samarage, C.R., Carberry, J., Sheard, G.J., and Fouras, A. (2012). Polynomial Element Velocimetry (PEV): A technique for continuous in-plane velocity and velocity gradient measurements for low Reynolds number flows. Meas. Sci. Technol. *23*, 105304.

Shamonin, D.P., Staring, M., Bakker, E., Xiao, C., Stolk, J., and Reiber, J.H.C. (2012). Automatic lung lobe segmentation of COPD patients using iterative B-spline fitting. Proc. S.P.I.E. *8314*, 83140W.

Steinberg, M.S. (2007). Differential adhesion in morphogenesis: a modern view. Curr. Opin. Genet. Dev. *17*, 281–286.

Stephenson, R.O., Yamanaka, Y., and Rossant, J. (2010). Disorganized epithelial polarity and excess trophectoderm cell fate in preimplantation embryos lacking E-cadherin. Development *137*, 3383–3391.

Strumpf, D., Mao, C.A., Yamanaka, Y., Ralston, A., Chawengsaksophak, K., Beck, F., and Rossant, J. (2005). Cdx2 is required for correct cell fate specification and differentiation of trophectoderm in the mouse blastocyst. Development *132*, 2093–2102.

Torres-Padilla, M.E., Parfitt, D.E., Kouzarides, T., and Zernicka-Goetz, M. (2007). Histone arginine methylation regulates pluripotency in the early mouse embryo. Nature *445*, 214–218.

Wadell, H. (1932). Volume, shape and roundness of rock particles. J. Geol. *40*, 443–451.

Watanabe, T., Biggins, J.S., Tannan, N.B., and Srinivas, S. (2014). Limited predictive value of blastomere angle of division in trophectoderm and inner cell mass specification. Development *141*, 2279–2288.

Wennekamp, S., Mesecke, S., Nédélec, F., and Hiiragi, T. (2013). A self-organization framework for symmetry breaking in the mammalian embryo. Nat. Rev. Mol. Cell Biol. *14*, 452–459.

Xiong, F., Ma, W., Hiscock, T.W., Mosaliganti, K.R., Tentner, A.R., Brakke, K.A., Rannou, N., Gelas, A., Souhait, L., Swinburne, I.A., et al. (2014). Interplay of cell shape and division orientation promotes robust morphogenesis of developing epithelia. Cell *159*, 415–427.

Yamanaka, Y., Ralston, A., Stephenson, R.O., and Rossant, J. (2006). Cell and molecular regulation of the mouse blastocyst. Dev. Dyn. *235*, 2301–2314.

Yamanaka, Y., Lanner, F., and Rossant, J. (2010). FGF signal-dependent segregation of primitive endoderm and epiblast in the mouse blastocyst. Development *137*, 715–724.

Yoshida, S., Barbier de Reuille, P., Lane, B., Bassel, G.W., Prusinkiewicz, P., Smith, R.S., and Weijers, D. (2014). Genetic control of plant development by overriding a geometric division rule. Dev. Cell *29*, 75–87.

Zernicka-Goetz, M., Morris, S.A., and Bruce, A.W. (2009). Making a firm decision: multifaceted regulation of cell fate in the early mouse embryo. Nat. Rev. Genet. *10*, 467–477.